Manganese metaphosphate $Mn(PO_3)_2$ as a high-performance negative electrode material for lithium-ion batteries

*Qingbo Xia[1,2], Pierre J.P. Naeyaert[1], Maxim Avdeev[1,2], Siegbert Schmid[1], Hongwei Liu[3], Bernt Johannessen[4], and Chris D. Ling[1, *]*

[1] School of Chemistry, The University of Sydney, Sydney 2006, Australia

[2] Australian Centre for Neutron Scattering, Australian Nuclear Science and Technology Organisation, Kirrawee 2232, Australia

[3] Australian Centre for Microscopy & Microanalysis, The University of Sydney, Sydney 2006, Australia

[4] Australian Synchrotron, Australian Nuclear Science and Technology Organisation, Clayton 3168, Australia

Abstract

We report a novel negative conversion electrode material, manganese (II) metaphosphate $Mn(PO_3)_2$. This compound can be synthesized by a facile solid-state method, and after carbon-coating delivers an attractively high reversible capacity of 477 mAh/g at 0.1C and 385 mAh/g at 1C. We investigated the reaction mechanism with a combination of *ex situ* X-ray absorption spectroscopy, *in situ* X-ray diffraction, and high-resolution transmission electron microscopy. We observed a direct conversion process by monitoring the first discharge *in operando*, in which $Mn(PO_3)_2$ reacts with Li to give fusiform Mn nanograins a few Ångstroms in width, embedded in a matrix of lithium conducting $LiPO_3$ glass. Due to the fine nanostructures of the conversion products, this conversion reaction is completely reversible.

Keywords: Lithium-ion batteries, conversion electrode, manganese (II) metaphosphate, nanograins.

Graphical Abstract

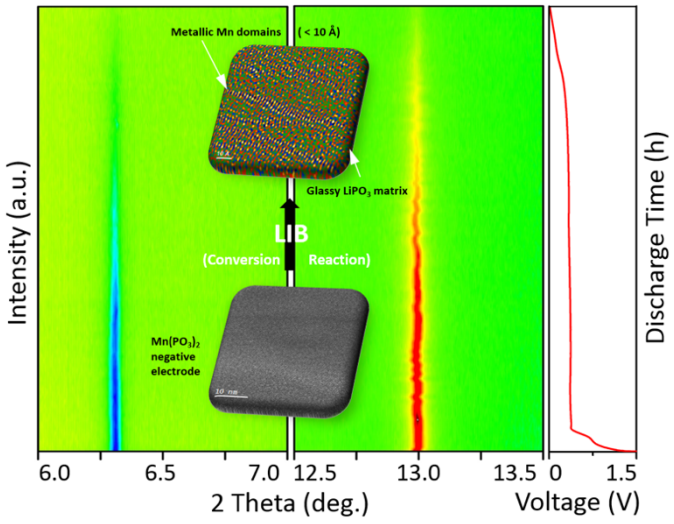

Introduction

Technology improvements in rechargeable batteries are currently being driven by the electric vehicle (EV) industry and smart-grid technologies based on renewable energy sources[1-5]. The former requires batteries with rapid charge and discharge rates, high energy densities, and high safety. For larger-scale applications, the latter requires batteries preferably with a low cost per kW h and which are environmentally friendly. Since lithium-ion batteries (LIBs) were commercialised in 1991[6], they have grown to dominate the rechargeable battery market by virtue of their performance and lifespan. They are now moving into new emerging applications such as EVs and grid-level power storage.

However, the electrode materials currently used in LIBs increasingly struggle to satisfy the demands of these new applications. This is particularly true of negative electrode materials[3, 6], where only a handful of choices are available, in contrast to the rich variety of positive electrode materials. There is also growing pressure to reduce the use of Co and Ni, the key metal elements in many commercial positive electrode materials (*e.g.*, $LiCoO_2$[7], $LiNi_{1-y-z}Mn_yCo_zO_2$[8]) and some state-of-the-art negative electrode materials (e.g., Co_3O_4[9], CoP[10], and NiP_3[11]), due to their toxicity, limited availability and rapidly increasing price[2, 12]. Discovering and developing new high energy density negative electrode materials based on naturally abundant elements (*e.g.*, Mn and Fe) is thus an urgent task for materials researchers.[13]

Graphitic carbon is the most common negative electrode material in commercial LIBs, theoretically delivering a relatively high capacity of 372 mAh/g through an intercalation reaction. However, it is intrinsically limited to modest practical capacity densities, especially when working at high rates[14], which is a serious shortcoming in EV applications. The capacity density of graphite, as in all intercalation electrode materials, is constrained by the crystal lattice. When Li intercalates in the lattice structure of the host, it occupies an interstitial site and blocks further Li ions from occupying directly adjacent interstitial sites, limiting the energy storage capacity, even though the active centre element (carbon or transition metals) in the host lattice could theoretically be further reduced.

Conversion reactions offer an alternative way forward to achieve higher energy capacity density, and they have attracted increasing attention in the last few years[15-18]. Conversion reactions enable transition metals to transfer two or more electrons and therefore can deliver more than double the capacity of regular intercalation reactions. Some oxides[19, 20], nitrides[21], phosphides[22], and sulphides[23] capable of reversibly storing Li through conversion reactions have been investigated as negative electrode candidates for LIBs. Complete reduction of transition metal ions in these compounds to the metallic state allows them to deliver very high capacities. However, issues related to electrochemical performances, such as rapid capacity fading upon cycling, low rate capability, and large irreversible capacity loss in the first cycle, have kept them from being commercialized[15, 18].

Far fewer conversion electrodes are known than intercalation materials. The search for new conversion materials has thus become an important area of research. Here we report the first systematic investigation of a novel negative conversion electrode material, manganese metaphosphate. In contrast to above monoanionic conversion materials with high-strength

ionic bonds, $Mn(PO_3)_2$ is a polyanionic compound with weaker ionic bonds and should therefore demonstrate higher electrochemical activity. In addition, $LiPO_3$, is formed through the conversion reaction and is also a good Li conductor, which should improve the intrinsic rate capability of manganese metaphosphate as an electrode. Finally, beyond exploring and quantifying the electrochemical properties of $Mn(PO_3)_2$, we have identified its conversion mechanism using synchrotron X-ray techniques combined with high-resolution transmission electron microscopy (HRTEM).

Experimental

Synthesis: Polycrystalline (powder) samples of manganese metaphosphate $Mn(PO_3)_2$ were synthesized by a conventional solid-state method. In a typical synthesis, stoichiometric manganese acetate tetrahydrate (AJAX, 99%) and ammonium di-hydrogen phosphate (BDH, 98%) were well ground and thoroughly mixed in a planetary ball-mill at 400 rpm for 2 h with acetone as the dispersant. After drying, the fine powder was placed in an alumina crucible and first heated in a muffle furnace at 400°C for 5h to remove volatile contents, followed by an intermediate grinding. The powder was heated again to 650°C and sintered at this temperature for 10 h to crystallize $Mn(PO_3)_2$. The obtained $Mn(PO_3)_2$ powder was finely ground before being used to make electrodes. Carbon-coating was performed by a carbothermic method in a tube furnace at 600°C for 3 h under Ar flow. A 1:1 (mass ratio) mixture of sucrose (Alfa Aesar, 99%) and PEG-6000 (Alfa Aesar) was selected as the carbon source to achieve a better coating effect. A 0.2:1 (mass ratio) mixture of carbon source and $Mn(PO_3)_2$ powder was thoroughly mixed in advance by wet ball milling at 400 rpm for 1 h. This procedure resulted in an integrally thin carbon coating layer of ~3nm on the surface of $Mn(PO_3)_2$ particle after carbothermic reduction, as shown in Figure 4b. The carbon content of as-prepared $Mn(PO_3)_2$/C is 6.72 *wt*%, measured by a GmbH-vario EL III Elemental Analyser.

Structural Characterization: Phase identity and purity of as-prepared $Mn(PO_3)_2$ and $Mn(PO_3)_2$/C were checked on a PANalytical X'Pert diffractometer. X-ray powder diffraction (XRD) data were collected from 10-70° (2θ) in reflection mode using Cu K_α monochromatic radiation (λ = 1.5406 Å). Rietveld refinement against XRD data was performed using TOPAS 5[24]. XRD patterns of the 1st lithiated and the 1st delithiated $Mn(PO_3)_2$ electrodes were also collected *ex situ* on the same instrument.

Electrochemical Characterization: The working electrode was prepared by casting the electrode slurry on a thick battery-grade copper foil (25 μm in thickness) with a loading density of 3 mg/cm^2. The slurry was made by homogeneously dispersing the active material powder ($Mn(PO_3)_2$ or $Mn(PO_3)_2$/C), carbon black (super P) (Alfa Aesar), and PVDF binder (polyvinylidene difluoride) (Aldrich) with a mass ratio of 80:10:10 in the solvent of NMP (1-methyl 2-pyrrolidinone) (Alfa Aesar). The electrode sheet was cut into round disks with a diameter of 16 mm after oven drying at 80°C, and then redried before being transferred into an Ar-filled glovebox. CR2032 half-cells were assembled in this glovebox using Li metal chips (MTI) as counter electrodes, Celgard polypropylene films (MTI) as separators, and 1M $LiPF_6$ (lithium hexafluorophosphate) solution (Sigma-Aldrich) in the mixed solvents of ethylene carbonate (EC) and diethyl carbonate (DEC) in a volume ratio of 50:50 as the electrolyte.

Half-cells were discharged and charged between 0.01 V and 2.5 V at room temperature on a Neware battery tester to evaluate the reversible capacity, cycling stability, and rate capability of the working electrode ($Mn(PO_3)_2$ or $Mn(PO_3)_2$/C). With our defined 1C current rate of 300 mA/g, we performed cycling measurements at 0.1C and performed variable rate measurements at 0.1C, 0.2C, 0.5C, 1C, 2C, 5C and 10C. A reference cell using carbon black as the working electrode was tested at variable rates (0.1-10C, 1C = 300 mA/g) in the voltage window of 0.01-2.5 V to evaluate the capacity contributions of carbon black to the observed capacities.

X-ray Absorption Spectroscopy: *Ex situ* X-ray absorption near-edge spectroscopy (XANES) measurements were performed on the XAS wiggler beamline (12ID) at the Australian Synchrotron. XANES spectra were acquired in transmission mode under a helium (He) atmosphere at room-temperature in the energy range around the Mn K-edge (E_0 = 6.5390 keV) from 6.350 keV to 7.090 keV. Instrument energy calibration was monitored using a bulk metallic Mn foil. Data processing was performed using the Demeter software suite[25]. A modified CR2032 coin cell was used in the XANES measurements, in which windows with a diameter of 4 mm were cut on the centre of both the top and bottom cases and the spacer to allow the beam to pass through the $Mn(PO_3)_2$ electrode. The coin cell of $Mn(PO_3)_2$ was cycled on a Neware battery tester near the beamline over an accumulated period of 18.8h. XANES spectra were collected from the same coin cell, which we transferred rapidly from the battery tester to the sample chamber in the beamline. This measurement approach reflects the state of the $Mn(PO_3)_2$ electrode in (close to) real-time during lithiation and de-lithiation which minimises experimental errors. XANES measurements were performed every two hours over the course of the 1st discharge and at the end of the 1st charge. A current rate of 0.2C was used for both discharge and charge processes.

Synchrotron XRD: *In situ* XRD measurements were carried out in transmission mode at the Powder Diffraction beamline at the Australian Synchrotron. Continuous measurements during only the first discharge process were collected at λ = 0.6888 Å over a 2θ range of 1.5–76.5° with each total diffraction pattern measured over a period of 4mins. The similar experimental coin cell to the one used in the XANES measurement was discharged with a Neware battery tester at a current rate of 0.2C during the measurements.

Electron Microscopy: The textures and microstructures of $Mn(PO_3)_2$ particles before and after the 1st lithiation and pristine $Mn(PO_3)_2$/C particles were characterized with a JEOL JEM-2200FS transmission electron microscope (TEM). The lithiated electrode was washed three times with dimethyl carbonate (DMC) in an argon atmosphere before being dispersed in ethanol and loaded onto specialised TEM copper mesh.

Results and Discussion

Manganese metaphosphate $Mn(PO_3)_2$ crystallizes in the monoclinic space group C1 2/c 1[26]. Its framework structure, shown in Figures 1a-b, consists of edge-sharing [MnO_6] zig-zag octahedral chains and [P_4O_{12}] rings which are alternately stacked perpendicularly to the [010] axis. [MnO_6] chains run approximately along the [101] direction, while [P_4O_{12}] rings consisting

of four corner-sharing [PO_4] tetrahedra are isolated and distributed approximately parallel to the (010) planes. The XRD pattern in Figure 1c indicates that single-phase crystalline $Mn(PO_3)_2$ was obtained from the solid-state reaction synthesis. Rietveld refinement against XRD data yielded an excellent profile fit with R_{wp} = 4.83%. No structural difference was apparent from the XRD pattern after carbon-coating, see Figure S1.

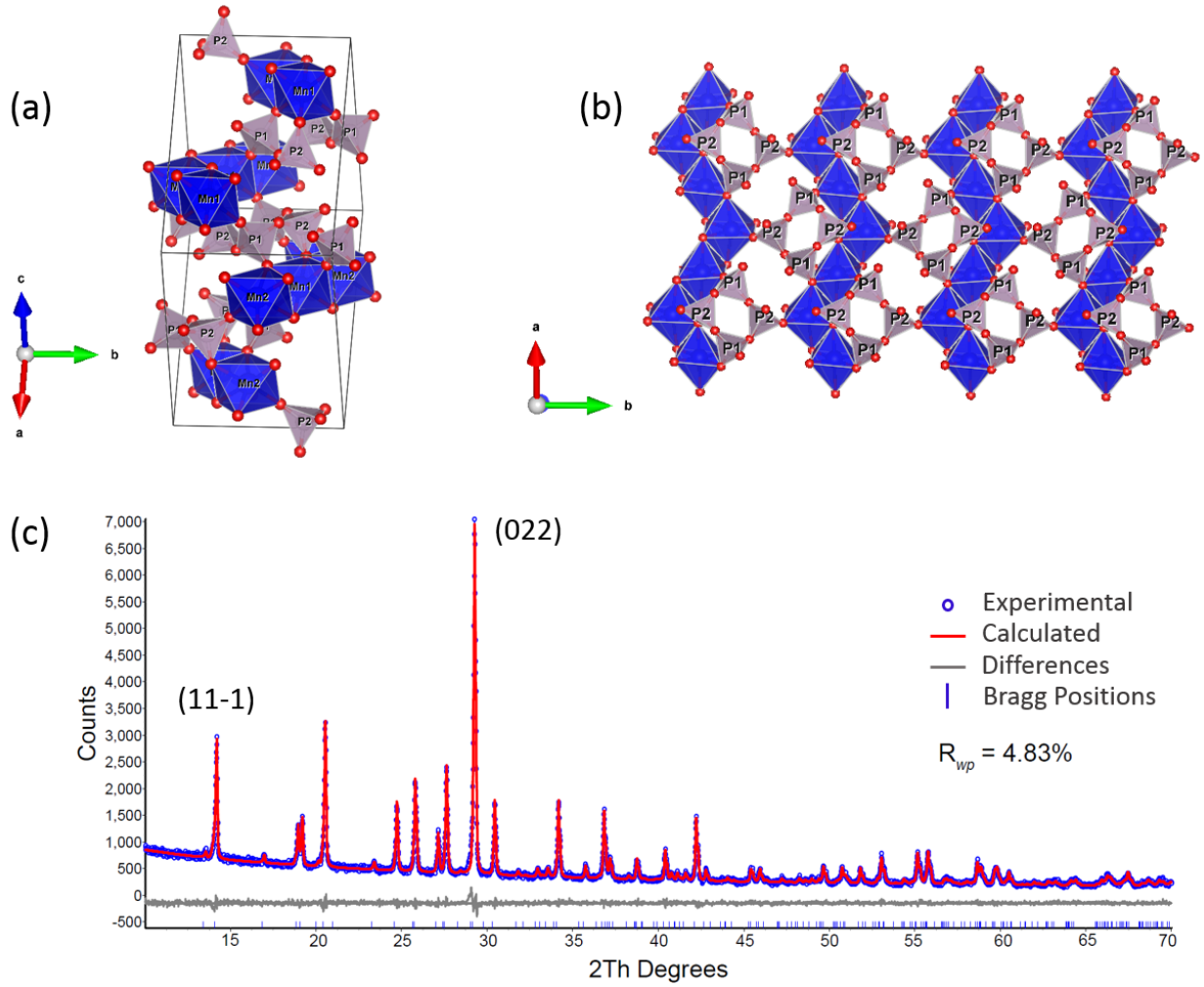

Figure 1 (a) The unit cell of monoclinic $Mn(PO_3)_2$ and (b) a projection of the crystal structure of $Mn(PO_3)_2$ on the (110) plane. (c) Rietveld-refinement against the XRD pattern (λ = 1.5406 Å) of as-prepared $Mn(PO_3)_2$.

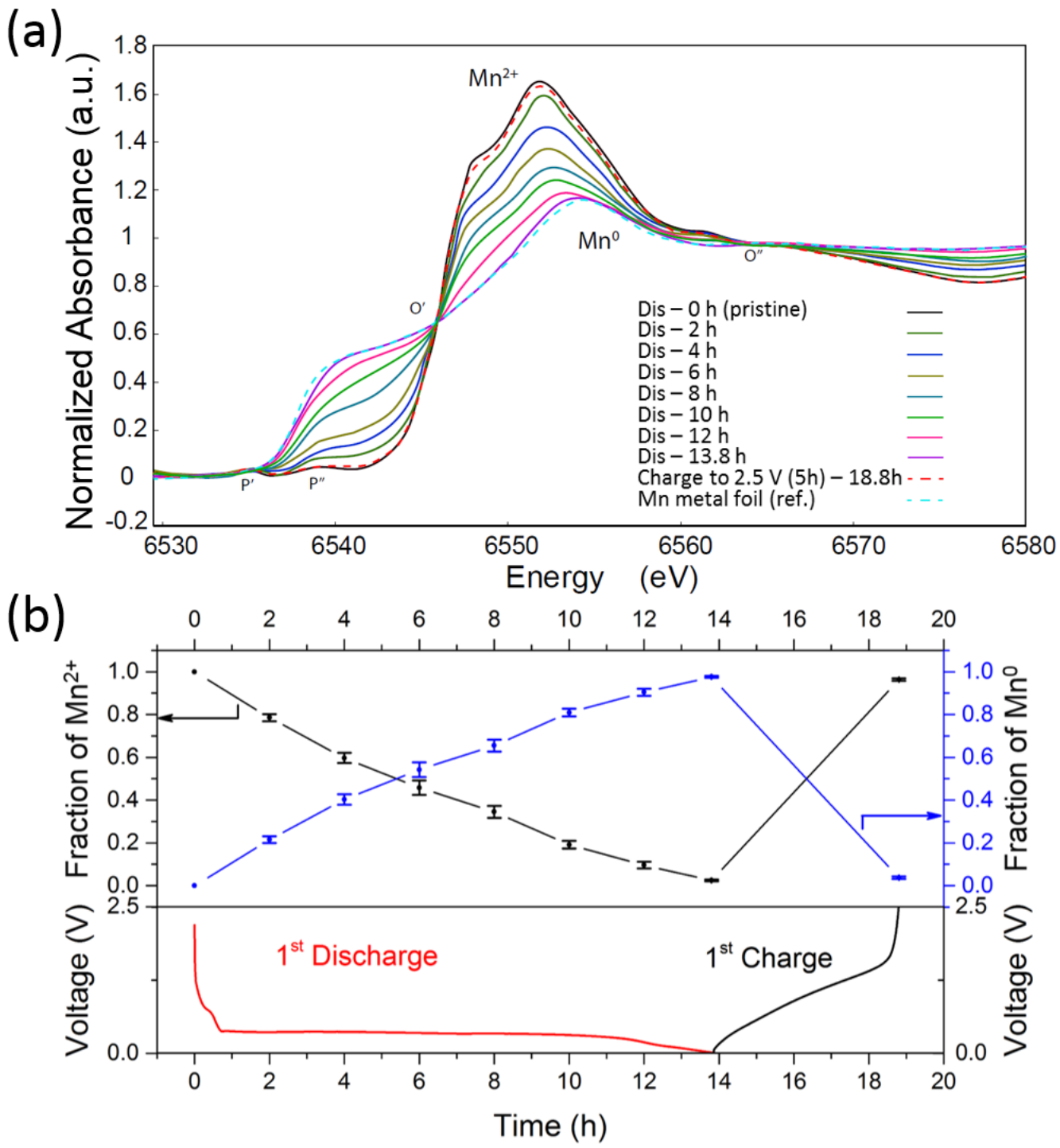

Figure 2 (a) *Ex situ* XANES spectra of the $Mn(PO_3)_2$ electrode during the 1st discharge (Mn reduction) and after 1st charge (Mn oxidation). (b) Fraction of Mn^{2+} / Mn^0 (with error bars) as a function of time, as determined from XANES spectra obtained by linear combination fitting.

The electrochemical reaction of $Mn(PO_3)_2$ with Li was first examined using the XANES technique which is sensitive to the local bonding environment and oxidation state[27]. Mn K-edge *ex situ* XANES spectra were collected during the first discharge and charge processes

are presented in Figure 2a. As can be seen, there are two isosbestic points O' and O'' at 6546 eV and 6564 eV respectively in the XANES spectra. This indicates a two-phase redox reaction. A typical Mn^{2+} absorption spectrum obtained from the pristine electrode is similar to the reported Mn K-edge spectra from manganese (II) oxide[28, 29].

Two small peaks at 6535 eV and 6539 eV in the pre-peak region are observed in the XANES spectrum of the pristine electrode which are due to transitions from the 1s core state to the 3d states[27].The first peak is caused by the local 1s3d quadrupole transition, while the second is produced by a dipole 1s4p transition (1s to the 4p character of the 3d-band due to the hybridization of the p and d orbitals).This second transition only occurs when Mn is oxidised (non-metallic state) as in $Mn(PO_3)_2$. A sharp upturn caused by the absorption of X-ray photons by the 1s electrons of Mn is observed, starting from 6542 eV and forming a shoulder at 6548 eV and a peak at 6552 eV in the spectrum of $Mn(PO_3)_2$. As the conversion reaction proceeds, the form of the collected spectra changes from Mn^{2+}-like to Mn^0-like with obvious position shifts of the 1s electron absorption shoulder and peak, and their decreasing intensities, approach those of metallic Mn. In the XANES spectrum of Mn metal foil (the reference), no peak is observed in the pre-peak region, and the strong absorption shoulder and peak of 1s electrons are located at 6540 eV and 6554 eV, respectively, which is consistent with previous reports[30]. On the basis of these XANES spectra, the reversible conversion reaction which takes place in the $Mn(PO_3)_2$ electrode can be written as in Equation (1).

$$\mathrm{Mn^{2+}(PO_3)_2} + 2\,\mathrm{Li^+} + 2e^- \rightleftharpoons \mathrm{Mn^0} + 2\,\mathrm{Li^+PO_3} \qquad (1)$$

XANES spectra were fitted by linear combination fitting to calculate their corresponding fractions of Mn^{2+}/Mn^0 during the 1st discharge and 1st charge. The evolution of the fractions over time is shown in Figure 2b. The Mn^{2+} fraction linearly decreases over the discharge time of 13.8 h, indicating that the conversion reaction takes place continuously over this period. Almost all of the Mn^{2+} (0.976 ± 0.004) is reduced to Mn^0 by the end of discharging, and almost all of Mn^0 is oxidized back to Mn^{2+} (0.963 ± 0.006) in the following charge process, thus demonstrating that the conversion reaction in Equation (1) is completely reversible.

We then used *in situ* synchrotron XRD characterization to monitor the crystal structure evolution of the $Mn(PO_3)_2$ electrode during the 1st discharge process, see Figure 3. The (11-1) and (022) reflections of $Mn(PO_3)_2$ continuously lose intensity until they disappear at the end of the lithiation process. This is consistent with our results from *ex situ* XANES that the conversion reaction takes place continuously over the entire 1st discharge. XRD measurements did not provide evidences for the formation of intermediate phases, i.e., $Mn(PO_3)_2$ appears to convert directly to metallic Mn. At full lithiation, the $Mn(PO_3)_2$ electrode is too poorly crystalline to identify the conversion products by XRD. After a subsequent charge process, the electrode does not recrystallize as measured from the XRD pattern of the delithiated electrode, see Figure S2.

Unlike intercalation electrodes, which accommodate Li^+ ions in ordered crystal lattices, conversion materials require an amorphization process to activate the electrodes. This process is accompanied by a large volume expansion of the electrode particles, which adversely affects cycling stability through reduced contact with current collectors and conductive additives, and even pulverizes the particles themselves[17]. Some proposed

solutions to this problem have been shown to improve performance, such as fabricating nano-porous structures[10, 29], coating particle surfaces[29], compositing with flexible carbonaceous materials (*e.g.*, graphene[31]), and using flexible binders[32]. In the present work we found that carbon coating to form $Mn(PO_3)_2$/C greatly improved the electrochemical performance over short-term cycling.

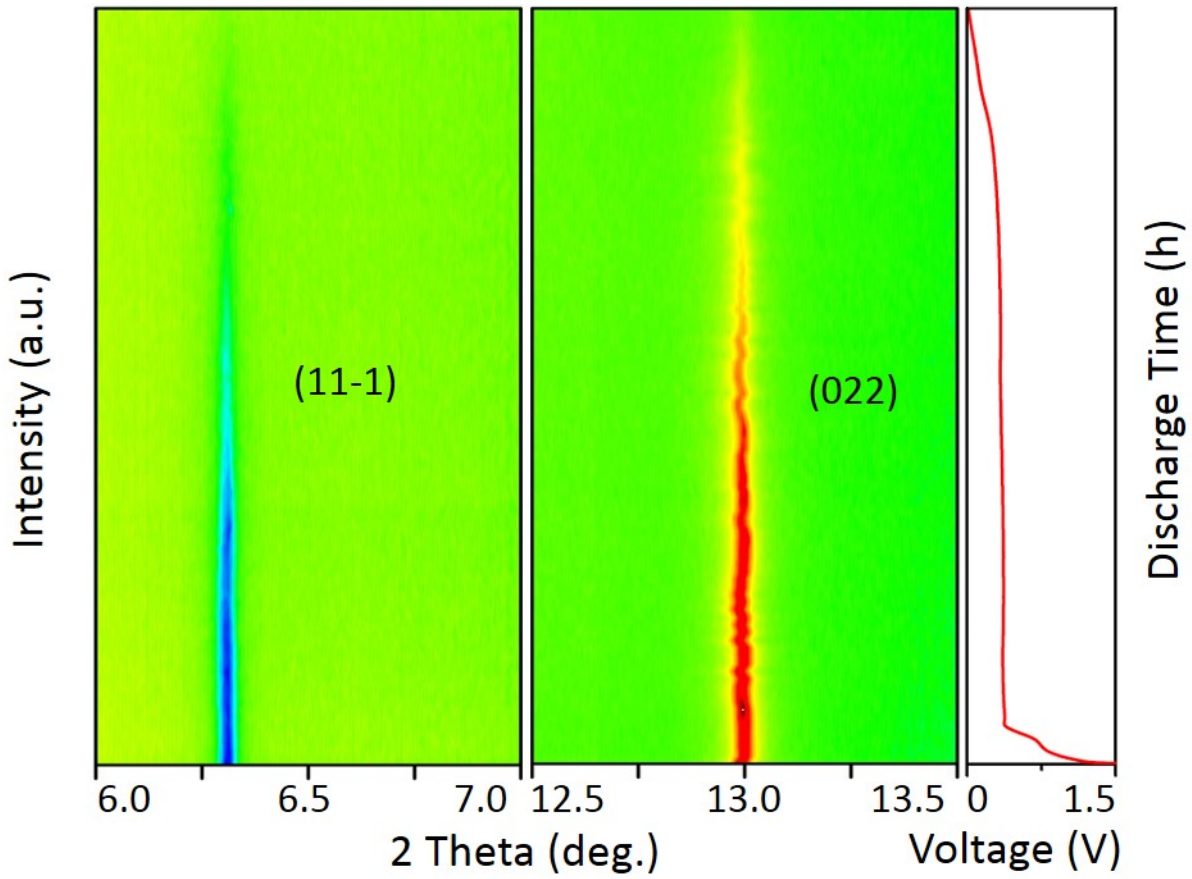

Figure 3 Selected 2θ regions of the *in situ* synchrotron XRD data (λ = 0.6888 Å) of the $Mn(PO_3)_2$ electrode during the 1st discharge.

The textural structure changes of the $Mn(PO_3)_2$ electrode before and after the conversion transformation were then locally examined by high-resolution transmission electron microscopy (HRTEM). As synthesized by the solid-state method at high temperature, both $Mn(PO_3)_2$ and $Mn(PO_3)_2$/C are highly crystalline, as evidenced by the long and continuous lattice fringes of the monoclinic metaphosphate structure in the HRTEM images in Figure 4a-b. Fine nanostructures were observed in lithiated $Mn(PO_3)_2$ particles, as shown in Figures 4c-d, with fusiform nanograins of several Ångstroms in width and several nanometres in length randomly dispersed in an amorphous matrix. The lattice fringe spacing of ~2.00 Å is consistent with metallic Mn, and can be indexed to the (411)/(330) planes of α-Mn[33] or the (221)/(310) of β-Mn[34] (*d*-spacings of α-Mn and β-Mn are shown in Table S1). α-Mn is the

most stable phase of manganese metal at room-temperature, with β-Mn normally only stable at high-temperatures, from 707-1087°C. However, as the width of the Mn nanograins formed here is smaller than the unit cells of both α-Mn and β-Mn (see Table 1), the structure cannot be conventionally labelled as either phase. This is further underlined by the significant defect concentration (missing or misplaced atoms) evident in Figure 4d.

The long axes of the Mn nanograins are mostly (but not perfectly) aligned, clearly retaining some of the orientation of the original crystalline $Mn(PO_3)_2$ from which they are nucleated. Their small size and homogenous dispersion throughout the glassy matrix create a percolation network, which enables efficient electron transfer through the electrode particles. This explains the ready re-conversion of lithiated $Mn(PO_3)_2$ electrode back to the delithiated form.

The amorphous matrix consists of glassy $LiPO_3$ according to Equation (1). $LiPO_3$ glass is an excellent lithium ion conductor and has been intensively investigated as a candidate solid-state electrolyte[35-37]. This leads to the expectation of good rate performance from our manganese metaphosphate electrodes.

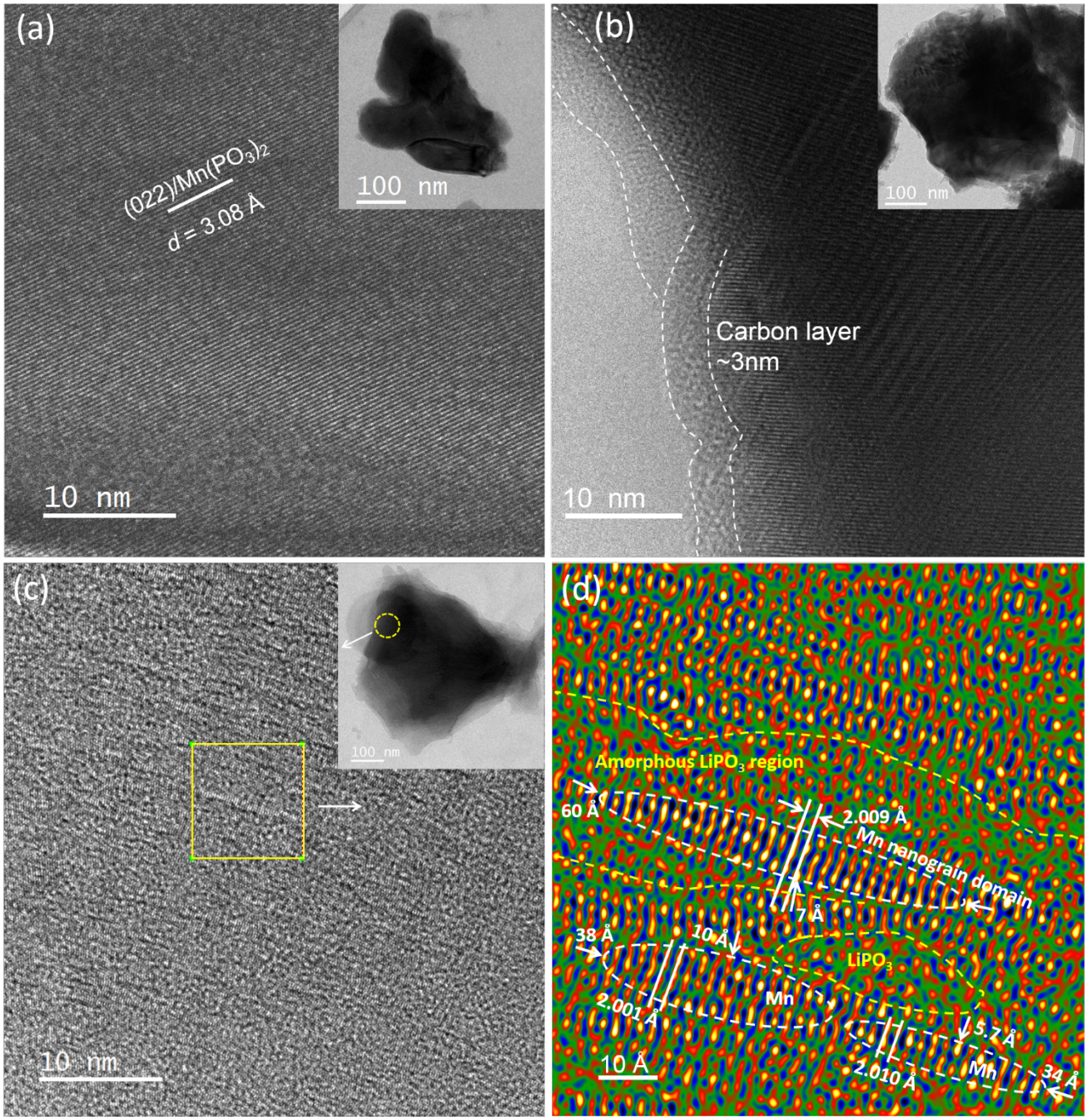

Figure 4 HRTEM images and bright-field images (inserts) of (a) as-prepared uncoated $Mn(PO_3)_2$ powders, (b) carbon coated $Mn(PO_3)_2$/C powders, and (c) fully lithiated $Mn(PO_3)_2$ electrode. (d) shows the inverse fast Fourier transform (IFFT) (coloured) of the yellow square area in (c).

Table 1 Cell parameters of α-Mn and β-Mn at the room temperature.

	Crystal System	Space Group	a (Å)	ICSD
α-Mn	Cubic	*I*-43*m*	8.911	# 42743
β-Mn	Cubic	$P4_132$	6.303	# 642934

Lastly, we evaluated the electrochemical performance of manganese metaphosphate as a negative electrode material in LIB half-cells. As shown in Figure 5a, an extraordinarily high initial discharge capacity of 831.8 mAh/g was obtained from the $Mn(PO_3)_2$ cell, more than triple the theoretical value (252 mAh/g) calculated from the conversion reaction in Equation (1). High reversible capacities up to ~321 mAh/g (from the 2nd discharge) were obtained in subsequent discharges, which is also ~70 mAh/g higher than the theoretical conversion value.

The extremely high capacity in the 1st discharge is due to irreversible decomposition of the electrolyte accompanied by the formation of a solid electrolyte interphase (SEI) film on the surface of the negative electrode particles. This process consumes a large amount of electrolyte, which therefore contributes considerable additional capacity. Further additional capacity in subsequent cycles is mainly due to "interfacial storage"[17] of lithium between Mn nanodomains and glassy $LiPO_3$ matrix, whereby additional Li^+ ions are stored on the glassy side while electrons are localized on the metallic side, leading to a formal charge separation[17]. Such two-phase pseudo-capacitive behaviour has been observed in many negative conversion electrodes[38, 39] and is also supported by theoretical calculations[40]. Note that the effect is particularly strong in this case because the interfacial area in this nanocomposite structure is so large.

Obvious differences are observed between the voltage profiles on 1st discharge and on subsequent discharges. This is due to the initial crystalline $Mn(PO_3)_2$ electrode which converts to an amorphous phase of the same composition after the 1st discharge. A long plateau at ~0.3 V in the 1st discharge curve reflects a steady two-phase transformation in which crystalline $Mn(PO_3)_2$ converts to $Mn/LiPO_3$ composite, as per our *in situ* XRD and TEM results. In the 2nd discharge curve, the amorphous phase of $Mn(PO_3)_2$ gives a steep voltage profile, in lieu of a plateau, which is consistent with the LIB half-cell behaving more like a capacitor. This is typical of conversion electrodes with large extra capacity caused by "interfacial storage"[19]. Voltage profiles of subsequent dis/charge cycles show the reversibility and relative stability of the electrochemistry of the amorphous phase. In comparison to the uncoated sample, the carbon-coated $Mn(PO_3)_2/C$ sample exhibits much higher electrochemical activity with a higher reversible capacity of ~477 mAh/g, as shown in the 2nd discharge in Figure 5b.The capacity increase between the samples before and after carbon coated is likely related to an enhancement of the "interfacial storage" of Li^+ ions. More Li^+ ions can be accommodated at the interfaces between Mn nanodomains and the glassy $LiPO_3$ matrix in lithiated $Mn(PO_3)_2/C$ due to its higher electron transfer kinetics, compared to uncoated samples; and additional Li^+ ions can be stored in the introduced interfaces between the amorphous carbon layer and the pseudo-amorphous $Mn/LiPO_3$ composite.

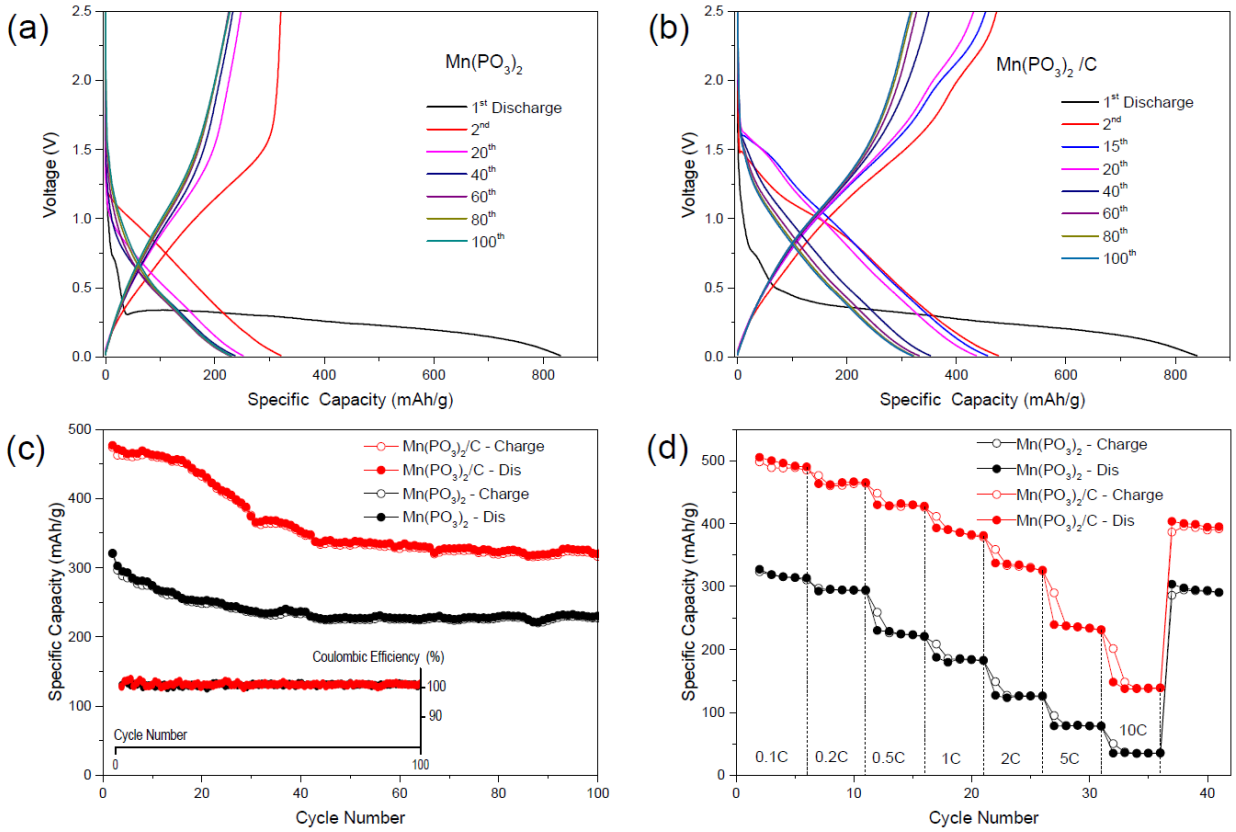

Figure 5 Electrochemical properties of uncoated $Mn(PO_3)_2$ and carbon-coated $Mn(PO_3)_2$/C. Voltage profiles of (a) $Mn(PO_3)_2$ and (b) $Mn(PO_3)_2$/C at 0.1C. (c) Cyclic performances (over 100 cycles) and (d) rate capabilities of both electrodes. All observed capacities include small contributions (see Figure S3 and Table S2) from the conductive additive carbon black in $Mn(PO_3)_2$ and $Mn(PO_3)_2$/C electrodes.

The cycling performance of both uncoated $Mn(PO_3)_2$ and carbon-coated $Mn(PO_3)_2$/C are compared in Figure 5c. The capacity of the $Mn(PO_3)_2$ electrode stabilized at ~230 mAh/g after a relatively rapid fading over the first 20 cycles with a capacity loss ratio 16.4% and a modest capacity retention ratio of 70.9% over 100 cycles. For the $Mn(PO_3)_2$/C electrode, a relatively small capacity fade over the first 15 cycles with a capacity loss ratio 1.8% was observed. This was followed by a rapid drop up to the 40th cycle with the capacity finally stabilizing at ~320 mAh/g for the remaining 60 cycles. The capacity retention ratio of $Mn(PO_3)_2$/C over 100 cycles is 68.3%, which is comparable to that of the uncoated $Mn(PO_3)_2$. Both materials show a high Coulombic efficiency approximately 100% during 100 cycles which demonstrates the complete reversibility of the lithium storage.

Carbon coating is a commonly used materials engineering strategy to improve electrochemical performances by increasing the electronic conductivity of the electrode and consequently enhancing the electrode reactivity. Carbon layers can also restrain volume variation during lithiation and de-lithiation processes which, to some extent can supress the particle pulverization (that results in significant capacity fading due to destroying the interfacial storage [17, 18]) in cycled conversion electrodes. As expected, much higher capacity is obtained

from carbon-coated $Mn(PO_3)_2$/C than the uncoated electrode material. Improved stability was also observed under short-term cycling compared to the uncoated $Mn(PO_3)_2$. The fast capacity fading between the 15th and 40th cycle observed for the $Mn(PO_3)_2$/C sample is likely caused by the limited ability of relatively rigid carbon-coated layers to $Mn(PO_3)_2$ particles to prevent cracking, or even pulverisation, due to the stress accumulated in previous cycles. After the 40th cycles, a new equilibrium state of stability capacity is reached after the stress has been relieved. Strategies such as nanostructured architectures, flexible surface coatings and solid-solutions have been demonstrated to supress the over-accumulation of stress in conversion electrode particles during long-term cycling, thereby prevent them from cracking and pulverising, leading to improved cycling performance of conversion electrodes.[15, 17-19] These can be explored in future works on manganese metaphosphate electrodes.

The rate capabilities of both uncoated $Mn(PO_3)_2$ and carbon-coated $Mn(PO_3)_2$/C were evaluated by charging and discharging the cells at various current rates. As shown in Figure 5d, attractively high reversible capacities of 460 mAh/g and 295 mAh/g at 0.2C, and 430 mAh/g and 225 mAh/g at 0.5C, were achieved for $Mn(PO_3)_2$/C and $Mn(PO_3)_2$, respectively. Even at a high rate of 5C, a remarkably high capacity of 235 mAh/g was obtained from carbon coated $Mn(PO_3)_2$/C. When the rate was returned to 0.1C, the original capacities of both electrodes were nearly fully recovered.

Conclusions

The electrochemical properties and working mechanisms of manganese (II) metaphosphate as a novel negative electrode material have been investigated for the first time. High reversible capacities at 0.1C of 321 mAh/g and 477 mAh/g were achieved for as-made $Mn(PO_3)_2$ and carbon-coated $Mn(PO_3)_2$/C, respectively. Both materials exhibit excellent rate capabilities, *e.g.*, 385 mAh/g at 1C and 330 mAh/g at 2C obtained from $Mn(PO_3)_2$/C. An ideal Coulombic efficiency of approximately 100% was obtained from both materials over 100 cycles which demonstrates that manganese (II) metaphosphate exhibits completely reversible Li^+ storage. However, while carbon-coating delivers higher capacities for $Mn(PO_3)_2$, its cycling performance is not effectively improved due to the stress-induced cracking of the rigid carbon film.

A combination of *ex situ* XANES, *in situ* synchrotron XRD, and HRTEM characterization draws a clear picture of the chemical, structural, and texture changes during discharge and charge. A direct conversion reaction takes place during the first lithiation, accompanied by the amorphization of crystalline $Mn(PO_3)_2$ and the formation of fusiform Mn nanograins less than 10 Å in width embedded in a glassy $LiPO_3$ matrix. The excellent lithium conductivity of this $LiPO_3$ glass, combined with the small size and homogeneous dispersion of the Mn nanograins, lead to both high reversibility and fast kinetics for the conversion reaction. Finally, we note that manganese metaphosphate is based on the naturally abundant element Mn and can be synthesised easily by a facile solid-state method. All these features make it an appealing candidate for use in new LIBs for emerging applications.

Supporting Information

Figure S1 Comparison of XRD patterns of uncoated $Mn(PO_3)_2$ and carbon coated $Mn(PO_3)_2$/C.

Figure S2 XRD patterns of the 1st lithiated and the 1st delithiated amorphous $Mn(PO_3)_2$ electrodes.

Table S1 *d*-spacings of α-Mn and β-Mn at room temperature.

Figure S3 Voltage profiles of carbon black at various current rates in the voltage range of 0.01-2.5V.

Table S2 Capacity contributions of carbon black to the observed capacities from manganese metaphosphate electrodes at various current rates.

Acknowledgements

This work was supported by the Australian Research Council – Discovery Projects program (DP170100269). Q. X. thanks ANSTO and Sydney Nano Institute for scholarship support.

References

[1] M. A. Hannan, M. S. H. Lipu, A. Hussain, A. Mohamed, *Renew Sust Energ Rev* **2017**, 78, 834.
[2] D. Larcher, J. M. Tarascon, *Nat Chem* **2015**, 7, 19.
[3] N. Nitta, F. X. Wu, J. T. Lee, G. Yushin, *Mater Today* **2015**, 18, 252.
[4] G. Zubi, R. Dufo-Lopez, M. Carvalho, G. Pasaoglu, *Renew Sust Energ Rev* **2018**, 89, 292.
[5] R. Schmuch, R. Wagner, G. Horpel, T. Placke, M. Winter, *Nat Energy* **2018**, 3, 267.
[6] G. E. Blomgren, *J Electrochem Soc* **2017**, 164, A5019.
[7] L. J. Liu, L. Q. Chen, X. J. Huang, X. Q. Yang, W. S. Yoon, H. S. Lee, J. McBreen, *J Electrochem Soc* **2004**, 151, A1344.
[8] O. Dolotko, A. Senyshyn, M. J. Muhlbauer, K. Nikolowski, H. Ehrenberg, *J Power Sources* **2014**, 255, 197.
[9] X. N. Leng, S. F. Wei, Z. H. Jiang, J. S. Lian, G. Y. Wang, Q. Jiang, *Sci Rep-Uk* **2015**, 5.
[10] B. Wang, Q. Ru, Q. Guo, X. Q. Chen, Z. Wang, X. H. Hou, S. J. Hu, *Eur J Inorg Chem* **2017**, DOI: 10.1002/ejic.2017006163729.
[11] J. Fullenwarth, A. Darwiche, A. Soares, B. Donnadieu, L. Monconduit, *J Mater Chem A* **2014**, 2, 2050.
[12] C. P. Grey, J. M. Tarascon, *Nat Mater* **2017**, 16, 45.
[13] B. Dunn, H. Kamath, J. M. Tarascon, *Science* **2011**, 334, 928.
[14] V. Etacheri, R. Marom, R. Elazari, G. Salitra, D. Aurbach, *Energ Environ Sci* **2011**, 4, 3243.
[15] M. V. Reddy, G. V. S. Rao, B. V. R. Chowdari, *Chem Rev* **2013**, 113, 5364.
[16] F. Wang, R. Robert, N. A. Chernova, N. Pereira, F. Omenya, F. Badway, X. Hua, M. Ruotolo, R. G. Zhang, L. J. Wu, V. Volkov, D. Su, B. Key, M. S. Whittingharn, C. P. Grey, G. G. Amatucci, Y. M. Zhu, J. Graetz, *J Am Chem Soc* **2011**, 133, 18828.
[17] J. Cabana, L. Monconduit, D. Larcher, M. R. Palacin, *Adv Mater* **2010**, 22, E170.
[18] A. Kraytsberg, Y. Ein-Eli, *J Solid State Electr* **2017**, 21, 1907.
[19] A. Sarkar, L. Velasco, D. Wang, Q. S. Wang, G. Talasila, L. de Biasi, C. Kubel, T. Brezesinski, S. S. Bhattacharya, H. Hahn, B. Breitung, *Nat Commun* **2018**, 9.
[20] L. L. Luo, J. S. Wu, J. M. Xu, V. P. Dravid, *Acs Nano* **2014**, 8, 11560.
[21] D. Zhang, G. S. Li, M. J. Yu, J. M. Fan, B. Y. Li, L. P. Li, *J Power Sources* **2018**, 384, 34.

[22] D. Yang, J. X. Zhu, X. H. Rui, H. T. Tan, R. Cai, H. E. Hoster, D. Y. W. Yu, H. H. Hng, Q. Y. Yan, *Acs Appl Mater Inter* **2013**, 5, 1093.
[23] L. Fei, Q. L. Lin, B. Yuan, G. Chen, P. Xie, Y. L. Li, Y. Xu, S. G. Deng, S. Smirnov, H. M. Luo, *Acs Appl Mater Inter* **2013**, 5, 5330.
[24] A. A. Coelho, J. S. O. Evans, I. R. Evans, A. Kern, S. Parsons, *Powder Diffr* **2011**, 26, S22.
[25] B. Ravel, M. Newville, *J Synchrotron Radiat* **2005**, 12, 537.
[26] R. Glaum, H. Thauern, A. Schmidt, M. Gerk, *Z Anorg Allg Chem* **2002**, 628, 2800.
[27] G. S. Henderson, F. M. F. de Groot, B. J. A. Moulton, *Rev Mineral Geochem* **2014**, 78, 75.
[28] K. W. Nam, M. G. Kim, K. B. Kim, *J Phys Chem C* **2007**, 111, 749.
[29] K. F. Zhong, B. Zhang, S. H. Luo, W. Wen, H. Li, X. J. Huang, L. Q. Chen, *J Power Sources* **2011**, 196, 6802.
[30] G. N. Greaves, P. J. Durham, G. Diakun, P. Quinn, *Nature* **1981**, 294, 139.
[31] X. Y. Cai, L. F. Lai, Z. X. Shen, J. Y. Lin, *J Mater Chem A* **2017**, 5, 15423.
[32] S. S. Zhang, *J Electrochem Soc* **2012**, 159, A1226.
[33] J. A. Oberteuffer, J. A. Ibers, *Acta Crystall B-Stru* **1970**, B 26, 1499.
[34] G. D. Preston, *Philos Mag* **1928**, 5, 1207.
[35] E. Kartini, T. Y. S. P. Putra, I. Kuntoro, T. Sakuma, K. Basar, O. Kamishima, J. Kawamura, *J Phys Soc Jpn* **2010**, 79, 54.
[36] E. Kartini, M. Nakamura, M. Arai, Y. Inamura, K. Nakajima, T. Maksum, W. Honggowiranto, T. Y. S. P. Putra, *Solid State Ionics* **2014**, 262, 833.
[37] P. Hockicko, J. Kudelcik, F. Munoz, L. Munoz-Senovilla, *Adv Electr Electron* **2015**, 13, 198.
[38] S. Laruelle, S. Grugeon, P. Poizot, M. Dolle, L. Dupont, J. M. Tarascon, *J Electrochem Soc* **2002**, 149, A627.
[39] X. Zhao, Q. C. Zhuang, S. D. Xu, Y. X. Xu, Y. L. Shi, X. X. Zhang, *J Electrochem Soc* **2015**, 162, A1156.
[40] Y. F. Zhukovskii, E. A. Kotomin, P. Balaya, J. Maier, *Solid State Sci* **2008**, 10, 491.